


ORIGINAL ARTICLE

Open Access



# Three-dimensional multifrequency magnetic resonance elastography improves preoperative assessment of proliferative hepatocellular carcinoma

Guixue Liu<sup>1†</sup>, Di Ma<sup>2†</sup>, Huafeng Wang<sup>3†</sup>, Jiahao Zhou<sup>1</sup>, Zhehan Shen<sup>1</sup>, Yuchen Yang<sup>2</sup>, Yongjun Chen<sup>2</sup>, Ingolf Sack<sup>4</sup>, Jing Guo<sup>4</sup>, Ruokun Li<sup>1\*</sup> and Fuhua Yan<sup>1\*</sup> 

## Abstract

**Background** To investigate the viscoelastic signatures of proliferative hepatocellular carcinoma (HCC) using three-dimensional (3D) magnetic resonance elastography (MRE).

**Methods** This prospective study included 121 patients with 124 HCCs as training cohort, and validation cohort included 33 HCCs. They all underwent preoperative conventional magnetic resonance imaging (MRI) and tomoelastography based on 3D multifrequency MRE. Viscoelastic parameters of the tumor and liver were quantified as shear wave speed ( $c$ , m/s) and loss angle ( $\varphi$ , rad), representing stiffness and fluidity, respectively. Five MRI features were evaluated. Multivariate logistic regression analyses were used to determine predictors of proliferative HCC to construct corresponding nomograms.

**Results** In training cohort, model 1 (Combining cirrhosis, hepatitis virus, rim APHE, peritumoral enhancement, and tumor margin) yielded an area under the curve (AUC), sensitivity, specificity, accuracy of 0.72, 58.73%, 78.69%, 67.74%, respectively. When adding MRE properties (tumor  $c$  and tumor  $\varphi$ ), established model 2, the AUC increased to 0.81 (95% CI 0.72–0.87), with sensitivity, specificity, accuracy of 71.43%, 81.97%, 75%, respectively. The C-index of nomogram of model 2 was 0.81, showing good performance for proliferative HCC. Therefore, integrating tumor  $c$  and tumor  $\varphi$  can significantly improve the performance of preoperative diagnosis of proliferative HCC (AUC increased from 0.72 to 0.81,  $p = 0.012$ ). The same finding was observed in the validation cohort, with AUC increasing from 0.62 to 0.77 ( $p = 0.021$ ).

**Conclusions** Proliferative HCC exhibits low stiffness and high fluidity. Adding MRE properties (tumor  $c$  and tumor  $\varphi$ ) can improve performance of conventional MRI for preoperative diagnosis of proliferative HCC.

**Critical relevance statement** We investigated the viscoelastic signatures of proliferative hepatocellular carcinoma (HCC) using three-dimensional (3D) magnetic resonance elastography (MRE), and find that adding MRE properties (tumor  $c$  and tumor  $\varphi$ ) can improve performance of conventional MRI for preoperative diagnosis of proliferative HCC.

<sup>†</sup>Guixue Liu, Di Ma and Huafeng Wang are contributed equally to this work as first authors

\*Correspondence:

Ruokun Li

lrk12113@rjh.com.cn

Fuhua Yan

yfh11655@rjh.com.cn

Full list of author information is available at the end of the article

**Key points**

1. HCC demonstrates a distinct viscoelasticity signature on 3D MRE.
2. Proliferative HCC exhibits low stiffness and high fluidity.
3. Combining MRE properties can improve the preoperative diagnostic performance of proliferative HCC.

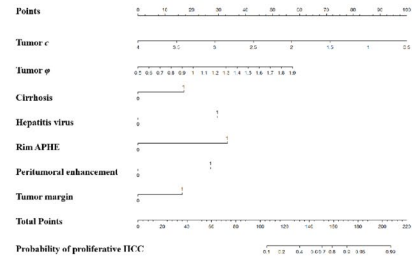
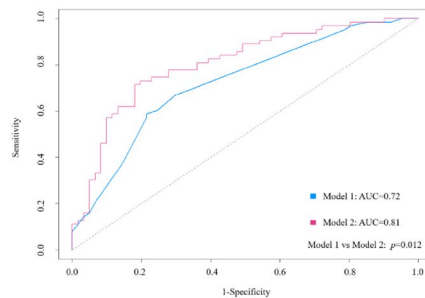
**Keywords** Hepatocellular carcinoma, Proliferative, Magnetic resonance elastography, Magnetic resonance imaging

**Graphical Abstract**

Three-dimensional multifrequency magnetic resonance elastography improves preoperative assessment of proliferative hepatocellular carcinoma



- HCC demonstrates a distinct viscoelasticity signature on 3D MRE.
- Proliferative HCC exhibits low stiffness and high fluidity.
- Combining MRE properties can improve the preoperative diagnostic performance of proliferative HCC.



**We investigated the viscoelastic signatures of proliferative hepatocellular carcinoma (HCC) using three-dimensional (3D) magnetic resonance elastography (MRE), and find that adding MRE properties (tumor  $c$  and tumor  $\phi$ ) can improve performance of conventional MRI for preoperative diagnosis of proliferative HCC.**

Insights Imaging (2023) Liu G, Ma D, Wang H et al. DOI: 10.1186/s13244-023-01427-4

**Background**

Hepatocellular carcinoma (HCC) accounts for 90% of primary liver cancers and is the second most common cause of cancer-related deaths worldwide [1]. HCC exhibits a highly heterogeneous phenotype at the molecular and histologic levels [2, 3]. By integrating morphology and molecular alterations, HCC can be classified as either the proliferative (~50%) or non-proliferative (~50%) phenotype [2, 4]. Each proliferation class is characterized by activation of varied genomic pathways related to cellular proliferation and survival (e.g., *AKT/mTOR*, *MET*, *TGF- $\beta$* , and insulin-like growth factor pathways), high rates of chromosomal instability, and aberrant epigenetic changes [2, 5]. Compared with non-proliferative HCC, proliferative HCC demonstrates an invasive phenotype with moderate to poor cellular differentiation, frequent vascular invasion, high tumor recurrence, and a poor prognosis

[2, 5]. Therefore, identifying the aggressive HCC subtypes during pretherapeutic work-ups may have strong prognostic and therapeutic implications.

Recent studies have shown that imaging findings can be correlated with specific molecular traits of HCC. Histologically, proliferative HCCs include the progenitor, macrotrabecular, scirrhous, sarcomatoid, and neutrophil-rich types [6]. Progenitor-type HCC usually appears as targetoid dynamic enhancement patterns (LR-M), with more marked hypointensity on the hepatobiliary phase, lower apparent diffusion coefficients, and non-smooth tumor margins [7–9]. A recent study [10] showed that substantial necrosis, high serum AFP levels, and Barcelona Clinic Liver Cancer (BCLC) stage B or C were independent predictors of the macrotrabecular-massive (MTM)-HCC subtype; substantial necrosis helped identify MTM-HCCs with 65% sensitivity. Kang and Kim

et al. [11] evaluated the role of gadoxetate-enhanced MRI in differentiating proliferative from non-proliferative HCCs. These authors demonstrated that most proliferative HCCs showed rim APHE (61.9% vs 11.2% for non-proliferative HCCs), with 88.8% specificity. Combining rim APHE and a serum AFP (> 100 ng/mL) for diagnosing proliferative tumors increased the specificity to 98.3% (114/116). However, its sensitivity was 26.2%, which may be insufficient for clinical practice. Additionally, the sample did not include CK7-positive HCC (another significant proliferative type). Collectively, a comprehensive understanding of the imaging features of proliferative HCC remains limited.

Magnetic resonance elastography (MRE) allows noninvasively quantifying tissue mechanical properties in vivo and provides new insights into tumor biology. MRE has been developed to detect and characterize cancers, evaluate therapeutic responses, and investigate the underlying biophysical mechanisms associated with malignant transformation [12, 13]. Tomoelastography based on three-dimensional (3D) MRE techniques use multifrequency data acquisition and a wave-number-based inversion algorithm [14]. It yields highly resolved quantitative maps of shear wave speed ( $c$ , m/s) and loss angle ( $\phi$ , rad) as surrogates of tissue stiffness and fluidity, respectively [15]. 3D MRE can be used to noninvasively differentiate benign and malignant liver lesions [16] and detect pancreatic and prostate cancers [17, 18]. To our knowledge, the value of 3D MRE for predicting patients with proliferative HCC remains unknown.

Mechanical changes in the liver may be the source of genetic instability leading to tumor development, which can be used to explore the biological mechanism of liver tumor from the perspective of biomechanics [19]. Because proliferative HCC types exhibit underlying histological features, such as abundant fibrous stroma, rich necrotic components, and few tumor

pseudocapsules [7–9], we hypothesized that biomechanical properties are sensitive to structural composition and arrangements and may differ between proliferative and non-proliferative HCC. Here, we aimed to identify biomechanical features of proliferative HCCs using 3D MRE properties and developed MRE-based nomogram that can be used in patients with HCC for distinguishing the proliferative and non-proliferative HCC subtypes.

## Materials and methods

### Participants

The institutional review board of our hospital approved this prospective study (No. RJ2018-209), and all participants provided written informed consent. Two hundred seventy-three consecutive patients with focal liver lesions were included from July 2020 to November 2021 and were selected as the training cohort. One hundred fifty-two were excluded for the following reasons: non-HCC on pathology ( $n = 86$ ), lack of pathological results ( $n = 45$ ), suboptimal image quality ( $n = 15$ ), history of extrahepatic primary malignancies ( $n = 3$ ), and history of local or systemic therapy ( $n = 3$ ). Finally, 121 patients with 124 HCC lesions were included (Fig. 1a). Then, 33 HCC patients from December 2021 to September 2022 who met the above criteria were included as validation cohort (Fig. 1b). The time intervals between surgery and MRI examination were within 3 days.

### Conventional MRI

Conventional MRI examinations were performed on machines from three vendors (Magnetom Aera, Siemens, Germany; Ingenia, Philips, Netherlands; UN790, United Imaging, China) equipped with a dedicated 18-channel system. The liver imaging protocol included T1-weighted

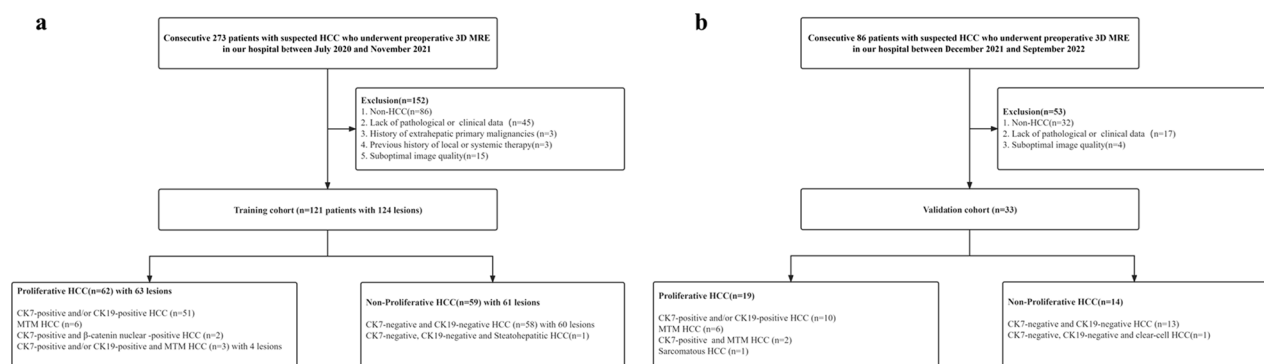


**Fig. 1** Flowchart of participant inclusions and exclusions. **a** Training cohort. **b** Validation cohort. HCC hepatocellular carcinoma; MTM macrotrabecular-massive

images (T1WI), T2-weighted images (T2WI), diffusion-weighted imaging (DWI) with b values of 0, 50 and 800 s/mm<sup>2</sup>, and gadolinium-diethylenetriaminepentaacetic acid (Gd-DTPA)-based dynamic contrast-enhanced (DCE) imaging. Additional file 1: Table S1 shows the imaging parameters for the MRI scanning protocol.

### 3D multifrequency MRE

3D multifrequency MRE was performed only on a 1.5-T MRI scanner (Magnetom Aera, Siemens, Erlangen, Germany) where MRE equipments are available. All patients fasted for at least 4 h prior to the examination. Our setup was similar to that described by Shahryari et al. [16]. Briefly, mechanical vibrations of 30, 40, 50 and 60 Hz were generated and transmitted to the liver using four surface-based pressure pads powered by compressed air. Two anterior and two posterior pads centered around the liver region were operated at 0.4 and 0.6 bar, respectively. The 3D wave fields were acquired by single-shot, spin-echo planar MRI sequencing with flow-compensated motion-coding gradients (MEGs).

As per Shahryari et al. [20], 15 contiguous slices with a field of view (FOV) of 312×384 mm<sup>2</sup>, matrix size of 104×128, and resolution of 3×3×5 mm<sup>3</sup> were obtained during free breathing. Further imaging parameters were repetition time (TR)=2050 ms; echo time (TE)=59 ms; parallel imaging with GRAPPA factor 2; MEG amplitude=30 mT/m; and MEG frequencies=43.48 Hz for 30, 40, and 50 Hz vibration frequencies and 44.88 Hz for 60 Hz vibration frequencies. The total acquisition time was approximately 3.5 min.

Multifrequency wave field data were processed using specialized software available at <https://bioqic-apps.com>. Finally, the FOV maps including shear wave speed ( $c$ ) and loss angle ( $\phi$ ) of the complex shear modulus were generated. As  $c$  is directly proportional to the square root of the storage modulus (the real part of the complex shear modulus), and  $\phi$  continuously changes from 0 (pure solid properties) to  $\pi/2$  (pure fluid property), these two parameters were considered substitutes for stiffness and tissue fluidity, respectively. Herein, we use  $c$  and  $\phi$  to describe quantitative information, and “stiffness” and “fluidity” to describe changes in qualitative parameters.

### Image analysis

Two experienced radiologists (reader 1 with 15 years of experience and reader 2 with 3 years of experience) reviewed all preoperative MRI features in consensus. For each lesion, the readers independently evaluated the following imaging features of each HCC: (a) rim arterial phase hyperenhancement (rim-APHE), defined as rim-like enhancement with relatively hypovascular central areas in the arterial phase [11, 22]; (b) nonperipheral

washout, defined as the reduction of overall or partial enhancement of nonperipheral visual assessment relative to composite liver parenchyma according to LI-RADS version 2018 [11, 21]; (c) capsule, defined as linear, thin and enhanced peripheral rim of smooth hyper-enhancement in the portal venous or delayed phase, according to LI-RADS version 2018 [21–23]; (d) peritumoral enhancement, defined as polygonal or crescent shaped enhancement that can be detected outside the tumor margin, which has a broad contact with the tumor boundary in the arterial phase, and shows same intensity with the background liver parenchyma in the equilibrium or portal venous phase [22, 23]; and (e) tumor margins which are defined at the equilibrium phase or portal venous phase can be divided into: smooth margin, showing as a nodular tumor with smooth contour; non-smooth tumor margin, presenting as non-smooth nodular tumors with focal extranodular growth [11, 22, 23]. If no consensus could be reached, a third reader (reader 3 with 32 years of experience) was consulted for the final decision.

For viscoelasticity measurements, the region of interest (ROI) was drawn manually based on magnitude images. A main slice showing the primary lesion at the maximum cross-sectional extension and two adjacent slices were selected to determine the ROIs. ROIs were defined to include only the tumor and liver parenchyma while avoiding the boundaries, tissue interface and large blood vessels. The readers were blinded to all clinical and laboratory information and histopathological results.

### Histopathological analysis

A pathologist with 15 years of experience who was blinded to all radiological and clinical results analyzed all specimens. Histomorphological subtypes were classified according to the World Health Organization (2019) [24]. Immunohistochemical staining for CK19 and CK7 was performed on representative tissue sections. When >5% of tumor cells expressed CK19, the HCC was determined to be CK19-positive [25]. When >5% of tumor cells were immunoreactive, they were considered CK7-positive [26]. When >50% of the tumor showed a major trabecular structural pattern, it was defined as MTM [5]. CK19-positive and CK7-positive, MTM, neutrophil-rich, sclerosing, and sarcomatous HCCs were classified as proliferative HCCs; CK19-negative and CK7-negative, steatohepatic, lymphocyte-rich, and clear-cell HCCs were classified as non-proliferative HCCs [2].

### Statistical analysis

For intergroup comparisons, continuous variables were tested using Student's t-test or the Mann–Whitney U test based on normality. Categorical variables were tested via the chi-square test or Fisher's exact test. Intraclass



correlation coefficients (ICCs) were used to test measurement consistency between two observers. Multivariate analysis with backward logistic regression was used to identify variables that were significantly and independently associated with proliferative HCC (dependent variable), and corresponding prediction nomograms were constructed. Variables included in the multivariate analysis were those significantly associated with proliferative HCC in the univariate analysis, as well as those thought to impact clinical outcomes, and included age, BMI, size, and MRE properties (tumor  $c$  and tumor  $\phi$ ) as continuous variables and sex, AFP, cirrhosis, hepatitis virus, major imaging features (rim APHE, nonperipheral washout, capsule, peritumoral enhancement, tumor margin), as dichotomous variables. Receiver operating characteristic curve analysis was performed to determine the diagnostic performance for predicting proliferative HCC. Decision curve analysis (DCA) was used to evaluate the clinical net benefits of the nomogram. All statistical analyses were performed using SPSS (version 26 for Windows; SPSS, Chicago IL, USA) and R (v4.0.5; URL <http://www.r-project.org>);  $p < 0.05$  was considered statistically significant.

## Results

### Demographic characteristics

In the training cohort, of 121 patients with 124 HCC lesions, 62 had proliferative HCC (mean age,  $58 \pm 12$  years; 51 men, 11 women, 63 lesions), and 59 had non-proliferative HCC (mean age,  $61 \pm 10$  years; 50 men, 9 women; 61 lesions). Cirrhosis differed significantly between proliferative and non-proliferative HCCs ( $p = 0.03$ ). The proliferative HCCs were significantly smaller than the non-proliferative HCCs ( $3.69 \pm 3.22$  vs.  $4.83 \pm 3.63$  cm,  $p = 0.01$ ). On histopathology, the proliferative HCCs were classified as CK7-positive (19.35%, 24/124), CK19-positive (10.48%, 13/124), CK7-positive and CK19-positive (11.29%, 14/124), MTM subtype (4.84%, 6/124), CK7-positive and  $\beta$ -catenin nuclear-positive (1.61%, 2/124), or CK7-positive and/or CK19-positive and MTM (3.23%, 4/124). The remaining HCCs were non-proliferative and included CK7-negative and CK19-negative HCCs (48.39%, 60/124), and CK7-negative, CK19-negative and steatohepatic HCCs (0.81%, 1 of 124). In the validation cohort, of 33 patients, 19 had proliferative HCCs (mean age,  $57 \pm 11$  years; 17 men, 2 women), and 14 had non-proliferative HCCs (mean age,  $55 \pm 11$  years; 12 men, 2 women). Size differed significantly between proliferative and non-proliferative HCCs ( $p = 0.021$ ). On histopathology, the proliferative HCCs were classified as CK7-positive (24.24%, 8/33), CK7-positive and CK19-positive (6.06%, 2/33), MTM subtype

(18.18%, 6/33), CK7-positive and MTM (6.06%, 2/33), sarcomatous HCCs (3.03%, 1/33). The remaining HCCs were non-proliferative and included CK7-negative and CK19-negative HCCs (39.39%, 13/33), and CK7-negative, CK19-negative and clear-cell HCCs (3.03%, 1 of 33). Table 1 describes the patients' clinicopathological characteristics. There were no significant differences in clinical characteristics between the training and validation cohorts (Additional file 1: Table S2).

### Major features and LI-RADS categories

In the training cohort, rim APHE ( $p = 0.02$ ) and LI-RADS categorization ( $p = 0.005$ ) differed significantly between proliferative and non-proliferative HCC. No significant differences were found for nonperipheral washout ( $p = 0.89$ ), capsule ( $p = 0.24$ ), peritumoral enhancement ( $p = 0.27$ ), or tumor margin ( $p = 0.09$ ). Figure 2 shows representative images of proliferative and non-proliferative HCCs. Table 2 lists the image features and LI-RADS categories.

### Viscoelasticity signatures of proliferative HCC

The ICCs were 0.96 (95% confidence interval [95% CI] 0.94–0.97) for tumor  $c$ , 0.88 (95% CI 0.84–0.92) for tumor  $\phi$ , 0.95 (95% CI 0.93–0.97) for liver  $c$ , and 0.89 (95% CI 0.84–0.92) for liver  $\phi$ , indicating good reproducibility (Additional file 1: Figure S1).

In the training cohort, Table 3 lists the biomechanical properties of proliferative and non-proliferative HCC. Tumor  $c$  was lower for proliferative HCC than for non-proliferative HCC ( $2.13 \pm 0.58$  vs.  $2.36 \pm 0.60$  m/s,  $p = 0.03$ ), indicating that proliferative HCCs were softer than were non-proliferative HCCs. However, tumor  $\phi$ , liver  $c$ , and liver  $\phi$  did not significantly differ between the two groups. 80.9% (51/63) of proliferative HCCs were progenitor-type (CK7- and/or CK19-positive). Further subgroup analysis between progenitor-type and non-progenitor-type HCCs showed similar results (Additional file 1: Table S3). Tumor  $c$  was lower for progenitor-type HCC than for non-progenitor-type HCC ( $2.10 \pm 0.60$  vs.  $2.36 \pm 0.61$  m/s,  $p = 0.02$ ). Tumor  $\phi$ , liver  $c$ , and liver  $\phi$  did not significantly differ between the subgroups.

### MRE-based prediction model for proliferative HCC

In the training cohort, univariate logistic regression analysis showed that tumor  $c$  (odds ratio [OR]: 0.51, 95% CI 0.27–0.95;  $p = 0.035$ ), cirrhosis (OR: 2.3, 95% CI 1.07–4.95;  $p = 0.033$ ), and rim APHE (OR: 4.55, 95% CI 1.22–17.03;  $p = 0.024$ ) were associated with proliferative HCC (Table 4). To adjust for confounding variables, multivariate analysis with backward stepwise regression showed that tumor  $c$  (OR: 0.15, 95% CI 0.05–0.43;  $p < 0.001$ ),

**Table 1** Comparison of the clinicopathological characteristics of proliferative and non-proliferative HCCs

Characteristic	Training cohort (n = 121)		p value	Validation cohort (n = 33)		p value
	Proliferative HCC (n = 62)	Non-proliferative HCC (n = 59)		Proliferative HCC (n = 19)	Non-proliferative HCC (n = 14)	
<i>Demographic</i>						
Age (years) (mean ± SD)	58 ± 12	61 ± 10	0.45	57 ± 11	55 ± 11	0.57
Sex (male: female)	51:11	50:9	0.71	17:2	12:2	0.74
BMI (kg/m <sup>2</sup> )	24.06 ± 3.2	23.85 ± 3.36	0.72	24.09 ± 2.88	24.96 ± 3.58	0.45
Cirrhosis	36 (58.06%)	46 (77.97%)	0.03*	14 (73.68%)	9 (64.29%)	0.56
Etiology			0.24			0.75
Hepatitis virus	56 (90.43%)	49 (83.05%)		14 (73.68%)	11 (78.57%)	
Non-hepatitis virus	6 (9.68%)	10 (16.95%)		5 (26.32%)	3 (21.43%)	
<i>Preoperative laboratory results</i>						
Albumin (g/dL)	39.77 ± 4.44	38.75 ± 6.12	0.08	37.84 ± 5.45	40.21 ± 2.42	0.14
Total bilirubin (μmol/L)	20.04 ± 14.96	18.87 ± 14.69	0.49	24.42 ± 15.03	17.31 ± 9.01	0.13
AFP (ng/mL)			0.99			0.89
≤ 100	42 (67.74%)	40 (67.80%)		14 (73.68%)	10 (71.43%)	
> 100	20 (32.26%)	19 (32.20%)		5 (26.32%)	4 (28.57%)	
CEA (ng/mL)			0.96			0.21
> 5	2 (3.23%)	2 (3.39%)		2 (10.53%)	0	
≤ 5	60 (96.77%)	57 (96.61%)		17 (89.47%)	14 (100%)	
CA125 (U/mL)			0.39			0.07
> 24	12 (19.35%)	8 (13.56%)		4 (21.05%)	0	
≤ 24	50 (80.65%)	51 (86.44%)		15 (78.95%)	14 (100%)	
CA199 (U/mL)			0.71			0.75
> 25	17 (27.42%)	18 (30.51%)		5 (26.32%)	3 (21.43%)	
≤ 25	45 (72.58%)	41 (69.49%)		14 (73.68%)	11 (78.57%)	
INR unit	1.055 ± 0.11	1.03 ± 0.11	0.12	1.08 ± 0.13	1.06 ± 0.07	0.87
ALT (IU/L)	42.52 ± 38.23	35.10 ± 43.79	0.28	54.37 ± 63.91	28.5 ± 13.37	0.22
AST (IU/L)	45.50 ± 42.36	44.81 ± 46.56	0.75	53.63 ± 63.17	28.57 ± 8.26	0.33
<i>HCC lesion features</i>						
Number of lesions	63	61		19	14	
Size (cm)	3.69 ± 3.22	4.83 ± 3.63	0.01*	4.55 ± 2.75	2.95 ± 2.98	0.021*

Data are the mean ± standard deviation or median and interquartile range (IQR) unless otherwise indicated

HCC hepatocellular carcinoma; BMI body mass index; AFP  $\alpha$ -fetoprotein; CEA carcinoembryonic antigen; CA125 carbohydrate antigen 125; CA199 Carbohydrate antigen 199; INR international normalized ratio of prothrombin time; ALT Alanine transaminase; AST Aspartate transaminase

\*Indicates statistically significant p values

tumor  $\phi$  (OR: 15.51, 95% CI 1.09–219.97;  $p=0.043$ ), cirrhosis (OR: 3.13, 95% CI 1.11–8.82;  $p=0.031$ ), hepatitis virus (OR: 7.16, 95% CI 1.59–32.25;  $p=0.01$ ), rim APHE (OR: 9.20, 95% CI 1.88–45.04;  $p=0.006$ ), peritumoral enhancement (OR: 6.07, 95% CI 1.32–27.87;  $p=0.02$ ), and tumor margin (OR: 2.98, 95% CI 1.12–7.95;  $p=0.029$ ) were independent factors for proliferative HCC (Fig. 3).

In training cohort, model 1 (Established using cirrhosis, hepatitis virus, rim APHE, peritumoral enhancement, and tumor margin) yielded an area under the curve (AUC), sensitivity, specificity, and accuracy of 0.72 (95% CI 0.64–0.80), 58.73 (95% CI 45.6–71.0), 78.69 (95% CI 66.3–88.1), and 68.55 (95% CI 58.76–75.85), respectively

(Fig. 4a). The C-index of the regression coefficient-based nomogram of model 1 was 0.72 (95% CI 0.64–0.80), showing good performance for predicting proliferative HCC (Fig. 5a). When adding MRE properties (tumor  $c$  and tumor  $\phi$ ), established model 2, the AUC increased to 0.81 (95% CI 0.72–0.87), with sensitivity, specificity, and accuracy of 71.43 (95% CI 58.7–82.1), 81.97 (95% CI 70.0–90.6), and 76.61 (95% CI 66.43–82.34), respectively (Fig. 4a). The C-index of the regression coefficient-based nomogram of model 2 was 0.81 (95% CI 0.72–0.87), showing good performance for predicting proliferative HCC (Fig. 5b). Therefore, integrating tumor  $c$  and tumor  $\phi$  can significantly improve the performance

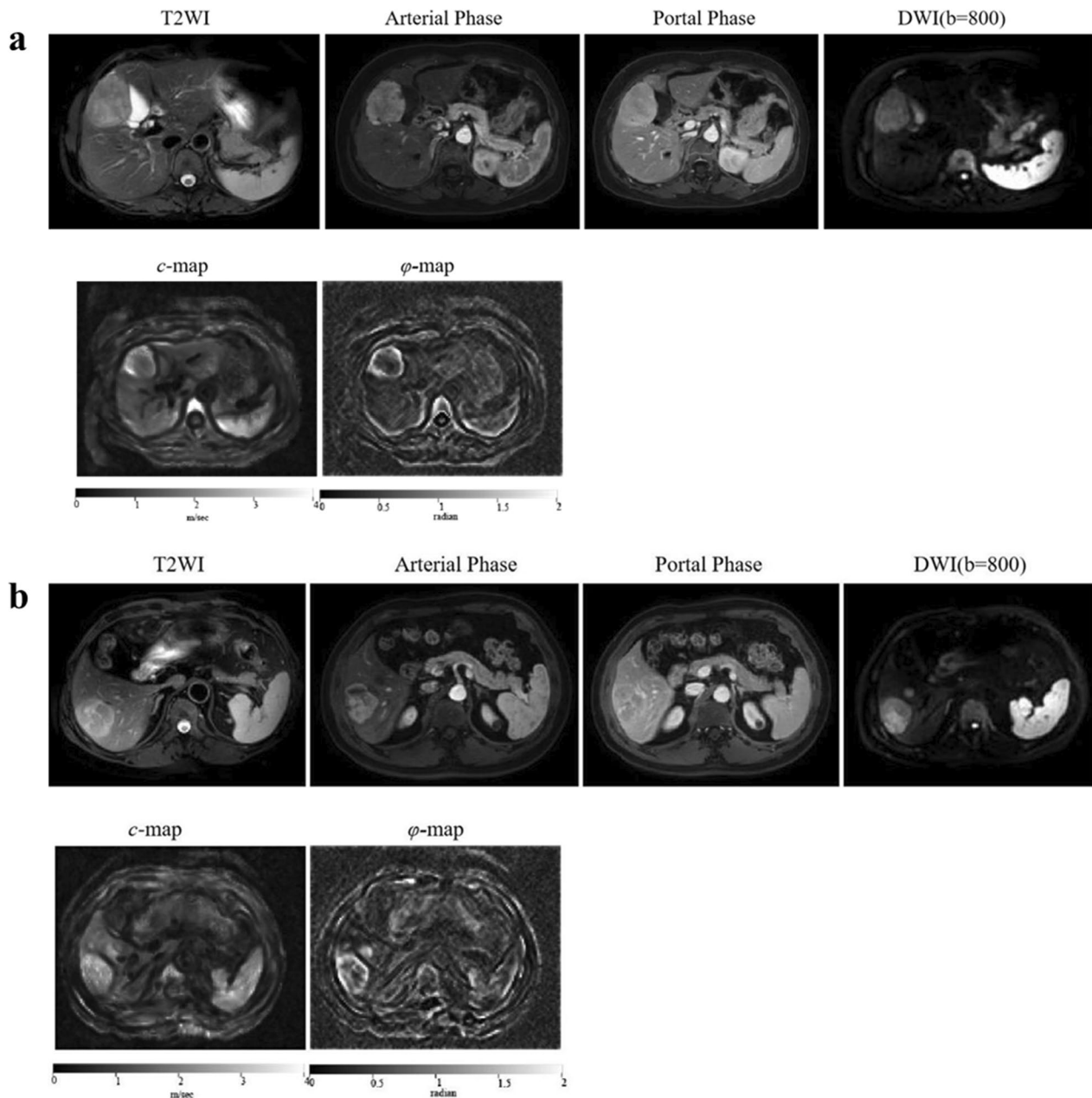


**Fig. 2** Representative patients' images. Axial T2-weighted images, arterial-phase images, portal-phase images, diffusion-weighted images at a b value of 800 s/mm<sup>2</sup>, axial c and  $\phi$  maps of tumors obtained in (a) a patient with proliferative HCC (tumor c: 2.31 m/s, tumor  $\phi$ : 1.23 rad, liver c: 1.91 m/s, and liver  $\phi$ : 0.68 rad) and (b) a patient with non-proliferative HCC (tumor c: 2.51 m/s, tumor  $\phi$ : 1.11 rad, liver c: 1.65 m/s, and liver  $\phi$ : 0.79 rad)

for preoperative diagnosis of proliferative HCC (AUC increased from 0.72 to 0.81,  $p=0.012$ , Fig. 4a). In the validation cohort, model 1 yielded AUC, sensitivity, specificity, and accuracy of 0.62 (95% CI 0.52–0.68), 63.16 (95% CI 50.03–75.43), 57.14 (95% CI 44.75–66.55), and 60.61 (95% CI 50.82–67.91), respectively (Fig. 4b). When adding MRE properties (tumor c and tumor  $\phi$ ), established

model 2, the AUC increased to 0.77 (95% CI 0.6–0.93), with sensitivity, specificity, and accuracy of 57.89 (95% CI 44.98–68.56), 85.71 (95% CI 73.74–94.34), and 69.70 (95% CI 59.52–75.43), respectively (Fig. 4b). So, integrating tumor c and tumor  $\phi$  can significantly improve the performance for preoperative diagnosis of proliferative HCC (AUC increased from 0.62 to 0.77,  $p=0.021$ , Fig. 4b). To

**Table 2** Major imaging features and LI-RADS categories for proliferative and non-proliferative HCC

	Proliferative HCC (n = 63)	Non-proliferative HCC (n = 61)	p value
Rim APHE			0.02*
Absent	51 (80.95%)	58 (95.08%)	
Present	12 (19.05%)	3 (4.92%)	
Nonperipheral washout			0.89
Absent	24 (38.10%)	24 (39.34%)	
Present	39 (61.90%)	37 (60.66%)	
Capsule			0.24
Absent	26 (41.27%)	19 (31.15%)	
Present	37 (58.73%)	42 (68.85%)	
Peritumoral enhancement			0.27
Absent	56 (88.89%)	50 (81.97%)	
Present	7 (11.11%)	11 (18.03%)	
Tumor margin			0.09
Smooth	33 (52.38%)	41 (67.21%)	
Non-smooth	30 (47.62%)	20 (32.79%)	
LR-RADS categorization			0.005*
LR-M	12 (19.05%)	3 (4.92%)	
LR-TIV	4 (6.35%)	1 (1.64%)	
LR-3	7 (11.11%)	2 (3.28%)	
LR-4	13 (20.63%)	10 (16.39%)	
LR-5	27 (42.86%)	45 (73.77%)	

APHE arterial-phase hyperenhancement; LI-RADS Liver Imaging Reporting & Data System; TIV tumor in vein

\*Indicates statistically significant p values

**Table 3** Mechanical parameters c (stiffness) and φ (fluidity) of proliferative and non-proliferative HCC

Parameters	Proliferative HCC (n = 63)	Non-proliferative HCC (n = 61)	p value
<i>Tumor</i>			
c (m/s)	2.13 ± 0.58	2.36 ± 0.60	0.03*
φ (rad)	1.08 ± 0.22	1.06 ± 0.21	0.64
<i>Liver</i>			
c (m/s)	1.94 ± 0.41	2.05 ± 0.42	0.18
φ (rad)	0.79 ± 0.12	0.77 ± 0.15	0.26

\*Indicates statistically significant p values

sum up, in both training and validation cohort, the AUC of model 2 was larger than that of model 1 (all  $p < 0.05$ ) (Fig. 4). The calibration curves of the nomograms showed good consistencies between the predicted and actual probability of proliferative HCCs in both training

**Table 4** Univariate and multivariate analysis of variables associated with proliferative HCC

	Univariate		Multivariate	
	OR (95% CI)	p value	OR (95% CI)	p value
Tumor c (m/s)	0.51 (0.27–0.95)	0.035*	0.15 (0.05–0.43)	<0.001*
Tumor φ (rad)	1.64 (0.31–8.63)	0.56	15.51 (1.09–219.97)	0.043*
<i>Sex</i>				
Female	1 (Reference)			
Male	0.93 (0.36–2.37)	0.87		
Age	0.98 (0.95–1.01)	0.27		
BMI	1 (0.9–1.11)	1.00		
Size	0.91 (0.82–1.02)	0.07		
<i>AFP (ng/mL)</i>				
≤ 100	1 (Reference)			
> 100	1.11 (0.52–2.35)	0.80		
<i>Cirrhosis</i>				
Absent	1 (Reference)			
Present	2.3 (1.07–4.95)	0.033*	3.13 (1.11–8.82)	0.031*
<i>Hepatitis virus</i>				
Absent	1 (Reference)			
Present	1.86 (0.63–5.49)	0.26	7.16 (1.59–32.25)	0.01*
<i>Rim APHE</i>				
Absent	1 (Reference)			
Present	4.55 (1.22–17.03)	0.024*	9.20 (1.88–45.04)	0.006*
<i>Nonperipheral Washout</i>				
Absent	1 (Reference)			
Present	1.05 (0.51–2.17)	0.89		
<i>Capsule</i>				
Absent	1 (Reference)			
Present	0.64 (0.31–1.35)	0.24		
<i>Peritumoral enhancement</i>				
Absent	1 (Reference)			
Present	1.76 (0.63–4.89)	0.28	6.074 (1.32–27.87)	0.02*
<i>Tumor margin</i>				
Smooth	1 (Reference)			
Non-smooth	1.86 (0.9–3.86)	0.094	2.98 (1.12–7.95)	0.029*

OR odds ratio; CI confidence interval; BMI body mass index; AFPα-fetoprotein; APHE arterial phase hyperenhancement

\*Indicates statistically significant p values

and validation cohorts of model 2 (Figs. 6a, b). In summary, the nomogram for predicting proliferative HCC in patients with HCC had considerable discriminative and calibrating abilities. In addition, decision curve analysis (DCA) was used to compare and visualize the clinical net benefits of the models (Fig. 6c, d) and showed that the model 2 gained more clinical net benefits than the model 1 in both training and validation cohorts.



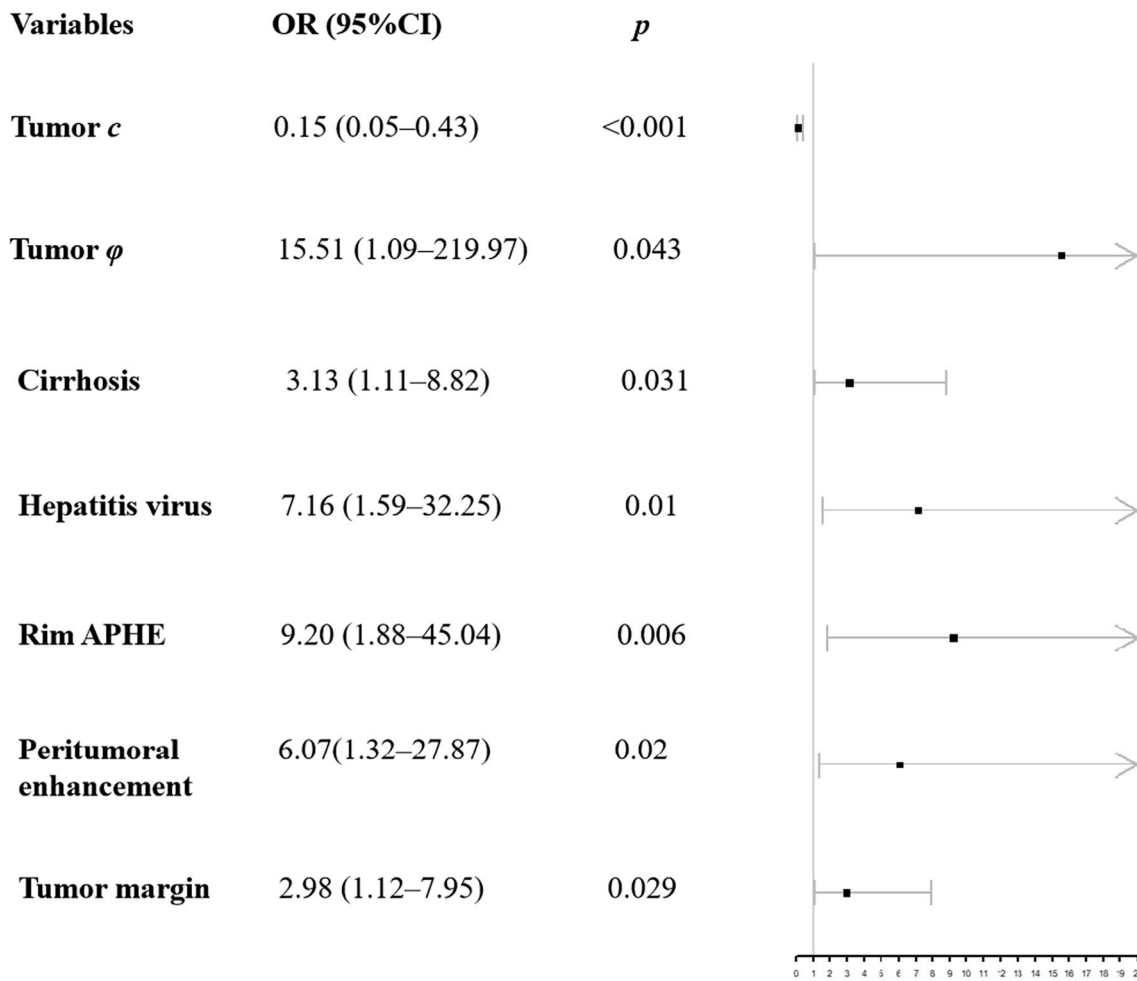


**Fig. 3** Forest plot of independent predictors of proliferative HCC with a multivariate regression model. Lines represent the 95%CI for tumor *c*, tumor  $\phi$ , cirrhosis, hepatitis virus, rim APHE, peritumoral enhancement, and tumor margin. Squares represent the OR for tumor *c*, tumor  $\phi$ , cirrhosis, hepatitis virus, rim APHE, peritumoral enhancement, and tumor margin. APHE: arterial phase hyperenhancement; OR: odds ratio; CI: confidence interval

**Discussion**

In this study, we investigated the viscoelastic signatures of proliferative HCC by 3D MRE. Our results showed that proliferative HCC had decreased tumor *c* and increased tumor  $\phi$  compared with those of non-proliferative HCC. MRE properties combined with conventional imaging and clinical features can significantly improve the performance for preoperative diagnosis of proliferative HCCs.

The softer mechanical signature of proliferative HCC in our study might be associated with its high metastatic potential and invasiveness. Studies have reported that during cancer progression, invasive and metastatic tumor cells may adaptively soften to facilitate and promote migration through narrow tissue space [27, 28]. Epithelial mesenchymal transformation was also reported to soften

cancer cells to infiltrate the matrix environment [29, 30]. Rianna et al. found that in 3D cultures, cells softened significantly during channel crossing, and the intracellular stiffness was negatively correlated with invasiveness [27]. The aforementioned mechanical alterations at the cellular level could be manifested collectively as macroscopic tumor softening, as shown here for proliferative HCCs. As reported [16], compared to benign lesions, malignant tumors behaved more fluid-like, showing stronger wave-attenuating properties as a result of changes in vasculature and extracellular matrix network organization, or the presence of necrotic tissue. Therefore, even if the univariate logistic regression analysis yielded no significant correlation, we included tumor  $\phi$  in the multivariate logistic regression analysis. In the multivariate analysis,

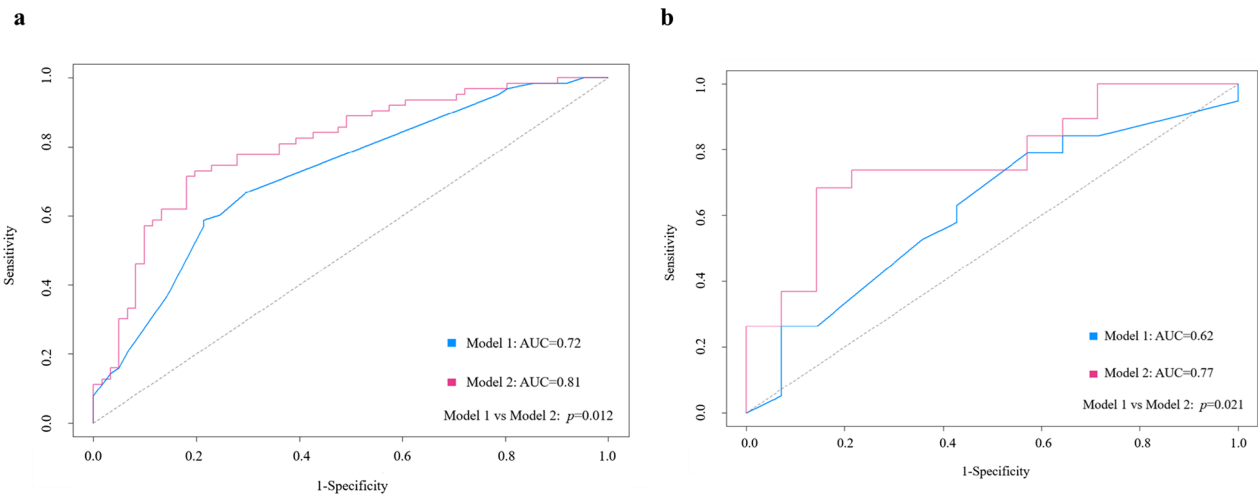


**Fig. 4** Area under the receiver operating characteristic curve for predicting proliferative HCC. **a** Model 1 (Combining cirrhosis, hepatitis virus, rim APHE, peritumoral enhancement, and tumor margin) and model 2 (Combining tumor  $c$ , tumor  $\phi$ , cirrhosis, hepatitis virus, rim APHE, peritumoral enhancement, and tumor margin) in the training cohort. **b** Model 1 and model 2 in the validation cohort. APHE: arterial phase hyperenhancement

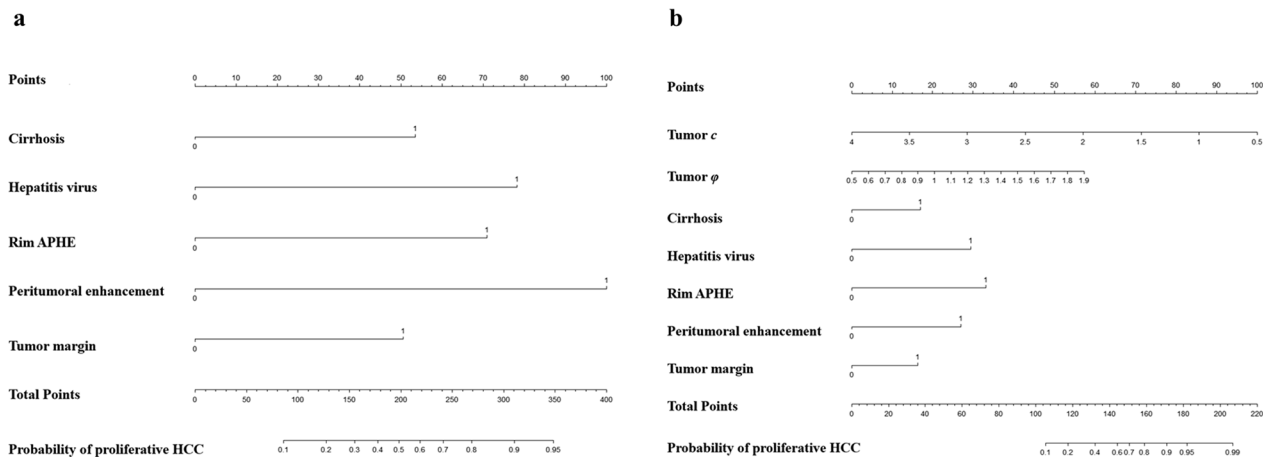


**Fig. 5** The nomograms yielded for prediction of proliferative HCCs. The nomograms of model 1 (**a**) (Combining cirrhosis, hepatitis virus, rim APHE, peritumoral enhancement, and tumor margin), and model 2 (**b**) (Combining tumor  $c$ , tumor  $\phi$ , cirrhosis, hepatitis virus, rim APHE, peritumoral enhancement, and tumor margin) for predicting proliferative HCCs. For cirrhosis, hepatitis virus, rim APHE, peritumoral enhancement, and tumor margin, “1” refers to presence. “Total Points” is the total score from adding all single scores obtained by variables of models, respectively. Single scores were obtained by drawing a line straight up from a single feature axis to the point axis. At the bottom of the scale, the points of all variables were added to obtain the prediction probability of proliferative HCCs. APHE: arterial phase hyperenhancement

tumor  $\phi$  was an independent predictor of proliferative HCC. That is, proliferative HCC behaved more fluidly than did non-proliferative HCC. Solid tumors become invasive through metastatic diffusion, which requires partial fluidization for cancer cells to migrate [16]. The increased fluidity may be related to angiogenesis, altered vascular density and increased mechanical friction [16].

Our results showed that cirrhosis is an independent risk factor associated with proliferative HCC. Increased

matrix rigidity can promote cancer cell survival, proliferation and migration [31]. Cirrhosis may promote HCC development by paving a collagen-rich rigid “highway” for cancer cell migration [32, 33]. Cirrhotic livers are reported to form immune-mediated cancer fields that contribute to HCC development, as shown by numerous gene signatures obtained from cirrhotic liver tissues [1, 34].

Consistent with previous reports, our results showed that rim APHE is another independent risk predictor of

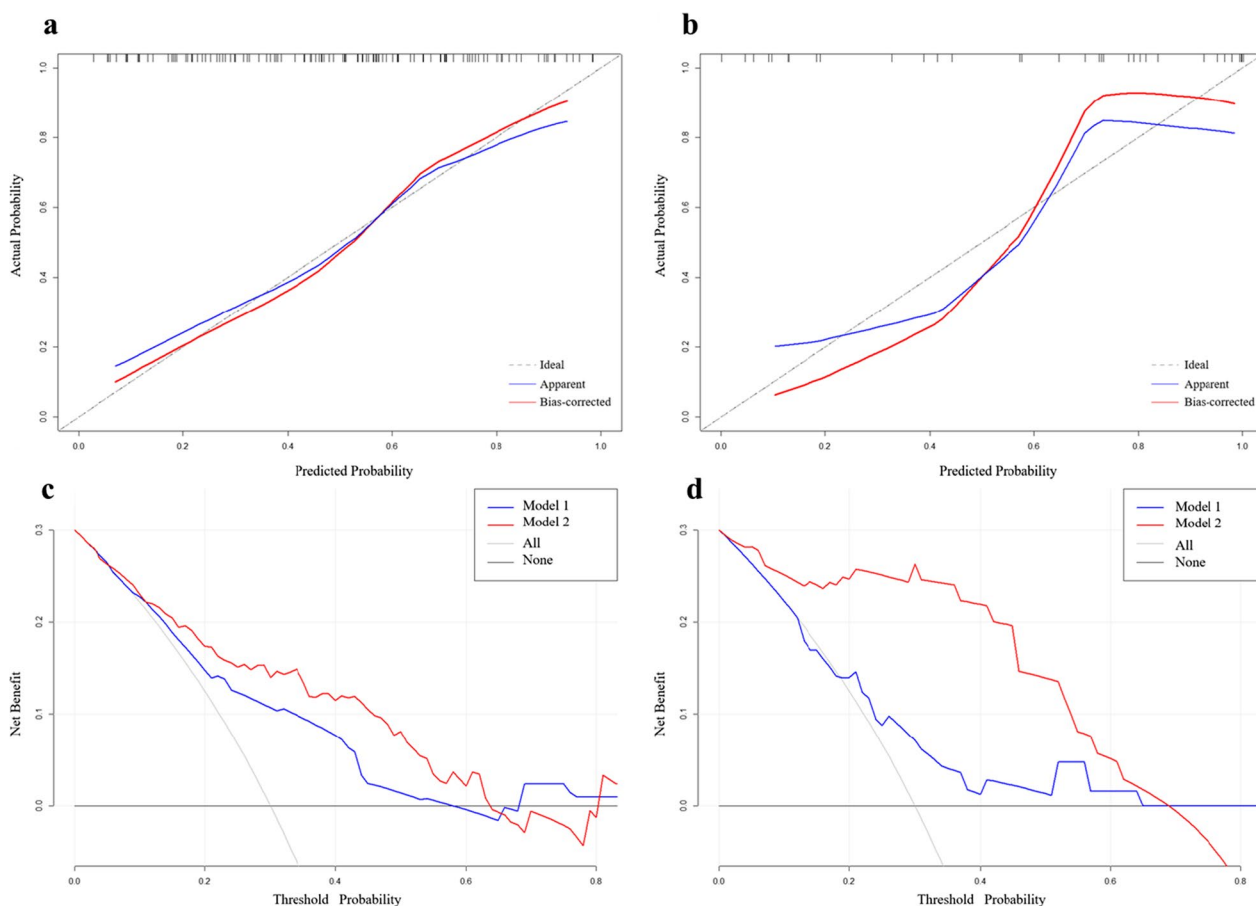


**Fig. 6** Calibration curves and decision curve analysis of the nomograms in the training and validation cohorts. Calibration curves for the estimation of model 2 (Combining tumor  $c$ , tumor  $\phi$ , cirrhosis, hepatitis virus, rim APHE, peritumoral enhancement, and tumor margin) predicted by the nomogram in the training cohort (a) and in the validation cohort (b). The x-axis indicates the predicted probability. The y-axis measures the actual probability. The blue line represents the performance of the nomogram, whereas the red line corrects for any bias in the nomogram. The dashed line represents the reference line where an ideal nomogram would lie. Decision curve analysis (DCA) of model 1 (Combining cirrhosis, hepatitis virus, rim APHE, peritumoral enhancement, and tumor margin) and model 2 in the training cohort (c) and in the validation cohort (d) indicated their clinical net benefits. The x-axis represents the threshold probability. The y-axis indicates the net benefit. The gray line shows the net benefit of proliferative HCCs. The blue and red lines represented model 1 and model 2 of nomograms, respectively. DCA indicated their clinical net benefits. DCA showed that the model 2 gained more clinical net benefit than the model 1 in both training and validation cohorts. APHE: arterial phase hyperenhancement

proliferative HCC. Kang and Kim et al. [11] reported that rim APHE was an independent predictor of proliferative HCC and more common in HCC with MTM, CK19-positive, scirrhous and sarcomatoid subtypes [10]. Rhee et al. [35] showed that HCC with rim APHE expressed higher levels of carbonic anhydrase IX and epithelial cell adhesion molecules, which were markers related to hypoxia and stemness, respectively. Rim APHE is related to poor differentiation, frequent microvascular invasion and a poor prognosis [36]. Additionally, most proliferative HCCs in our cohort were CK7-positive and/or CK19-positive. CK7 and CK19 are important markers of liver progenitor cells.

Thus, CK7-positive and CK19-positive HCC may have an intermediate phenotype between mature hepatocyte differentiation and the biliary tract during multistep hepatocarcinogenesis [25]. A previous study [35] confirmed that irregular rim-like enhanced HCC may express higher CK19 levels and demonstrate more invasive features.

Non-smooth tumor margins and peritumoral enhancement may reflect the aggressiveness of the HCC [22, 37, 38]. Therefore, even in the univariate logistic regression analysis, tumor margin and peritumoral enhancement were not significantly correlated with proliferative HCC, and we included these two image features in the multivariate

logistic regression analysis. The results showed that the non-smooth tumor margin and peritumoral enhancement were independent predictors of proliferative HCC. The non-smooth tumor margin on MRI is a feature of CK19-positive HCC [8, 35], which may be due to the tendency of HCC with a progenitor cell phenotype to have more aggressive growth types and higher histological grades, which may eventually lead to the appearance of non-smooth tumor margins [7]. Studies [39, 40] have shown that peritumoral enhancement is an independent predictor of higher pathological grades. Peritumoral enhancement is considered a useful imaging predictor for early recurrence of HCC after a hepatectomy [38]. Peritumoral enhancement is an important indicator to predict microvascular invasion (MVI) [22, 41–43], which may reflect changes in hemodynamic perfusion during compensatory arterial hyperperfusion [43].

Our study had several limitations. First, this was a single-center exploratory study. Further multicenter validation is needed. Second, our nomogram was established on patients with histologically proven HCC in the dominant areas of viral hepatitis, which limited the application of our nomogram to HCC cohorts only. To expand the clinical utility of our model, our nomogram will be updated in the future by including more HCCs with different etiologies as well as non-HCC lesions. Third, owing to the limited availability of MRE equipment, the clinical MRI examinations were performed on machines from three vendors. However, LI-RADS categories are based on qualitative interpretation of MRI and are system-independent. Finally, proliferative HCCs and non-proliferative HCCs were classified based on histopathological analyses. Further study based on genomic profiling is needed.

## Conclusion

In conclusion, proliferative HCC exhibits a distinct biomechanical signature of low stiffness and high fluidity compared with that of non-proliferative HCC. MRE properties combined with conventional imaging and clinical features can significantly improve the performance of conventional MRI for preoperative diagnosis of proliferative HCCs.

## Abbreviations

AFP	$\alpha$ -Fetoprotein
APHE	Arterial phase hyperenhancement
AUC	Area under the curve
HCC	Hepatocellular carcinoma
ICC	Intraclass correlation coefficient
MRE	Magnetic resonance elastography
MRI	Magnetic resonance imaging
MTM	Macrotrabecular-massive
OR	Odds ratio
ROI	Region of interest

## Supplementary Information

The online version contains supplementary material available at <https://doi.org/10.1186/s13244-023-01427-4>.

**Additional file 1. Supplementary Table 1.** Multiparametric MRI protocol. **Supplementary Table 2.** Demographics and clinical characteristics of the participants in this study. **Supplementary Table 3.** Mechanical parameters  $c$  (stiffness) and  $\phi$  (fluidity) of progenitor-type and non-progenitor-type HCC. **Supplementary Figure 1.** Bland-Altman plots of reader agreement. The  $c$  (a) and  $\phi$  (b) values of the tumor and  $c$  (c) and  $\phi$  (d) values of the liver.

## Acknowledgements

The authors acknowledge the Department of General Surgery at Ruijin Hospital (Shanghai Jiao Tong University School of Medicine, Shanghai, China) for assistance with patient information, surgical tumor tissue, and the Department of Pathology at Ruijin Hospital (Shanghai Jiao Tong University School of Medicine, Shanghai, China) for assistance with histological analysis. We acknowledge the Department of Radiology at Charité–Universitätsmedizin Berlin (Berlin, Germany) for assistance with technical support of MRE.

## Author contributions

GL contributed to data analysis and manuscript writing. DM contributed to data curation and revising the work. JZ, YY and YC contributed to data acquisition. HW contributed to the histopathological analysis. JG and IS contributed to interpreting the data and revising the work. RL and FY contributed to the conception, designing, and revising of the work. All authors read and approved the final manuscript.

## Funding

This study was supported by the Shanghai Science and Technology Foundation (21TS1400600) and the Deutsche Forschungsgemeinschaft (BIOQC GRK 2260 and SFB1340 Matrix-In-Vision).

## Availability of data and materials

The datasets used for analyses during the current study are available from the corresponding author on reasonable request.

## Declarations

### Ethics approval and consent to participate

The Ruijin Hospital Ethics Committee, Shanghai Jiaotong University School of Medicine (No. RJ2018-209) approved this prospective single-center cohort study.

### Consent for publication

All participants provided written informed consent.

### Competing interests

The authors declare that they have no competing interests.

### Author details

<sup>1</sup>Department of Radiology, Ruijin Hospital, Shanghai Jiao Tong University School of Medicine, No. 197 Ruijin Er Road, Shanghai 200025, China. <sup>2</sup>Department of General Surgery, Ruijin Hospital, Shanghai Jiao Tong University School of Medicine, Shanghai, China. <sup>3</sup>Department of Pathology, Ruijin Hospital, Shanghai Jiao Tong University School of Medicine, Shanghai, China. <sup>4</sup>Department of Radiology, Charité–Universitätsmedizin Berlin, Berlin, Germany.

Received: 1 December 2022 Accepted: 14 April 2023

Published online: 18 May 2023

## References

- Llovet JM, Kelley RK, Villanueva A et al (2021) Hepatocellular carcinoma. *Nat Rev Dis Prim* 7(1):6

2. Calderaro J, Ziol M, Paradis V, Zucman-Rossi J (2019) Molecular and histological correlations in liver cancer. *J Hepatol* 71(3):616–630
3. Nault JC, Martin Y, Caruso S et al (2020) Clinical impact of genomic diversity from early to advanced hepatocellular carcinoma. *Hepatology* 71(1):164–182
4. Zucman-Rossi J, Villanueva A, Nault JC, Llovet JM (2015) Genetic landscape and biomarkers of hepatocellular carcinoma. *Gastroenterology* 149(5):1226–1239 e1224
5. Calderaro J, Couchy G, Imbeaud S et al (2017) Histological subtypes of hepatocellular carcinoma are related to gene mutations and molecular tumour classification. *J Hepatol* 67(4):727–738
6. Durnez A, Verslype C, Nevens F et al (2006) The clinicopathological and prognostic relevance of cytokeratin 7 and 19 expression in hepatocellular carcinoma. A possible progenitor cell origin. *Histopathology* 49(2):138–151
7. Chen J, Wu Z, Xia C et al (2020) Noninvasive prediction of HCC with progenitor phenotype based on gadoxetic acid-enhanced MRI. *Eur Radiol* 30(2):1232–1242
8. Choi SY, Kim SH, Park CK et al (2018) Imaging features of gadoxetic acid-enhanced and diffusion-weighted MR imaging for identifying cytokeratin 19-positive hepatocellular carcinoma: a retrospective observational study. *Radiology* 286(3):897–908
9. Hu XX, Wang WT, Yang L et al (2019) MR features based on LI-RADS identify cytokeratin 19 status of hepatocellular carcinomas. *Eur J Radiol* 113:7–14
10. Mulé S, Galletto Pregliasco A, Tenenhaus A et al (2020) Multiphase liver MRI for identifying the macrotubercular-massive subtype of hepatocellular carcinoma. *Radiology* 295(3):562–571
11. Kang HJ, Kim H, Lee DH et al (2021) Gadoxetate-enhanced MRI features of proliferative hepatocellular carcinoma are prognostic after surgery. *Radiology* 300(3):572–582
12. Manduca A, Bayly PJ, Ehman RL et al (2021) MR elastography: principles, guidelines, and terminology. *Magn Reson Med* 85(5):2377–2390
13. Pepin KM, McGee KP (2018) Quantifying tumor stiffness with magnetic resonance elastography: the role of mechanical properties for detection, characterization, and treatment stratification in oncology. *Top Magn Reson Imaging* 27(5):353–362
14. Ingolf S (2022) Magnetic resonance elastography from fundamental soft-tissue mechanics to diagnostic imaging. *Nat Rev Phys* 5(1):25–42
15. Reiter R, Tzschätzsch H, Schwahofer F et al (2020) Diagnostic performance of tomoelastography of the liver and spleen for staging hepatic fibrosis. *Eur Radiol* 30(3):1719–1729
16. Shahryari M, Tzschätzsch H, Guo J et al (2019) Tomoelastography distinguishes noninvasively between benign and malignant liver lesions. *Can Res* 79(22):5704–5710
17. Gultekin E, Wetz C, Braun J et al (2021) Added value of tomoelastography for characterization of pancreatic neuroendocrine tumor aggressiveness based on stiffness. *Cancers (Basel)* 13(20):5185
18. Li M, Guo J, Hu P et al (2021) Tomoelastography based on multifrequency MR elastography for prostate cancer detection: comparison with multiparametric MRI. *Radiology* 299(2):362–370
19. Hu X, Zhou J, Li Y et al (2022) Added value of viscoelasticity for MRI-based prediction of Ki-67 expression of Hepatocellular Carcinoma using a deep learning combined radiomics (DLCR) model. *Cancers (Basel)* 14(11):2575
20. Shahryari M, Meyer T, Warmuth C et al (2021) Reduction of breathing artifacts in multifrequency magnetic resonance elastography of the abdomen. *Magn Reson Med* 85(4):1962–1973
21. Marrero JA, Kulik LM, Sirlin CB et al (2018) Diagnosis, staging, and management of hepatocellular carcinoma: 2018 practice guidance by the American Association for the study of liver diseases. *Hepatology* 68(2):723–750
22. Lee S, Kim SH, Lee JE, Sinn DH, Park CK (2017) Preoperative gadoxetic acid-enhanced MRI for predicting microvascular invasion in patients with single hepatocellular carcinoma. *J Hepatol* 67(3):526–534
23. Wei Y, Huang Z, Tang H et al (2019) IVIM improves preoperative assessment of microvascular invasion in HCC. *Eur Radiol* 29(10):5403–5414
24. Kim H, Jang M, Nyun PY (2020) Histopathological variants of hepatocellular carcinomas: an update according to the 5th edition of the WHO classification of digestive system tumors. *J Liver Cancer* 20(1):17–24
25. Wang W, Gu D, Wei J et al (2020) A radiomics-based biomarker for cytokeratin 19 status of hepatocellular carcinoma with gadoxetic acid-enhanced MRI. *Eur Radiol* 30(5):3004–3014
26. Geng Z, Zhang Y, Wang S et al (2021) Radiomics analysis of susceptibility weighted imaging for hepatocellular carcinoma: exploring the correlation between histopathology and radiomics features. *Magn Reson Med* 85(3):253–263
27. Rianna C, Radmacher M, Kumar S (2020) Direct evidence that tumor cells soften when navigating confined spaces. *Mol Biol Cell* 31(16):1726–1734
28. Rebelo LM, de Sousa JS, Mendes Filho J, Radmacher M (2013) Comparison of the viscoelastic properties of cells from different kidney cancer phenotypes measured with atomic force microscopy. *Nanotechnology* 24(5):055102
29. Chen YQ, Lan HY, Wu YC, Yang WH, Chiou A, Yang MH (2018) Epithelial-mesenchymal transition softens head and neck cancer cells to facilitate migration in 3D environments. *J Cell Mol Med* 22(8):3837–3846
30. Schrader J, Gordon-Walker TT, Aucott RL et al (2011) Matrix stiffness modulates proliferation, chemotherapeutic response, and dormancy in hepatocellular carcinoma cells. *Hepatology* 53(4):1192–1205
31. Mierke CT, Sauer F, Grosser S, Puder S, Fischer T, Käs JA (2018) The two faces of enhanced stroma: stroma acts as a tumor promoter and a steric obstacle. *NMR Biomed* 31(10):e3831
32. Ray A, Provenzano PP (2021) Aligned forces: origins and mechanisms of cancer dissemination guided by extracellular matrix architecture. *Curr Opin Cell Biol* 72:63–71
33. Egeblad M, Rasch MG, Weaver VM (2010) Dynamic interplay between the collagen scaffold and tumor evolution. *Curr Opin Cell Biol* 22(5):697–706
34. Moieni A, Torrecilla S, Tovar V et al (2019) An immune gene expression signature associated with development of human hepatocellular carcinoma identifies mice that respond to chemopreventive agents. *Gastroenterology* 157(5):1383–1397 e1311
35. Rhee H, An C, Kim HY, Yoo JE, Park YN, Kim MJ (2019) Hepatocellular carcinoma with irregular rim-like arterial phase hyperenhancement: more aggressive pathologic features. *Liver Cancer* 8(1):24–40
36. Murakami K, Kasajima A, Kawagishi N, Ohuchi N, Sasano H (2015) Microvessel density in hepatocellular carcinoma: prognostic significance and review of the previous published work. *Hepatol Res* 45(12):1185–1194
37. Banerjee S, Wang DS, Kim HJ et al (2015) A computed tomography radiogenomic biomarker predicts microvascular invasion and clinical outcomes in hepatocellular carcinoma. *Hepatology* 62(3):792–800
38. An C, Kim DW, Park YN, Chung YE, Rhee H, Kim MJ (2015) Single hepatocellular carcinoma preoperative MR imaging to predict early recurrence after curative resection. *Radiology* 276(2):433–443
39. Rong D, Liu W, Kuang S et al (2021) Preoperative prediction of pathologic grade of HCC on gadobenate dimeglumine-enhanced dynamic MRI. *Eur Radiol* 31(10):7584–7593
40. Chou YC, Lao IH, Hsieh PL et al (2019) Gadoxetic acid-enhanced magnetic resonance imaging can predict the pathologic stage of solitary hepatocellular carcinoma. *World J Gastroenterol* 25(21):2636–2649
41. Wang WT, Yang L, Yang ZX et al (2018) Assessment of microvascular invasion of hepatocellular carcinoma with diffusion kurtosis imaging. *Radiology* 286(2):571–580
42. Xu X, Zhang HL, Liu QP et al (2019) Radiomic analysis of contrast-enhanced CT predicts microvascular invasion and outcome in hepatocellular carcinoma. *J Hepatol* 70(6):1133–1144
43. Renzulli M, Brocchi S, Cucchetti A et al (2016) Can current preoperative imaging be used to detect microvascular invasion of hepatocellular carcinoma? *Radiology* 279(2):432–442

## Publisher's Note

Springer Nature remains neutral with regard to jurisdictional claims in published maps and institutional affiliations.